Published in final edited form as:
*J Am Chem Soc*. 2012 February 8; 134(5): 2750–2759. doi:10.1021/ja210400u.

# Discrete complexes immobilized onto Click-SBA-15 silica: Controllable loadings and the impact of surface coverage on catalysis

**Jun Nakazawa**, **Brian J. Smith**, and **T. Daniel P. Stack***
Department of Chemistry, Stanford University, Stanford, California 94305

## Abstract

Azidopropyl functionalized mesoporous silica SBA-15 were prepared with variable azide loadings of 0.03 – 0.7 mmol $g^{-1}$ (*ca*. 2 – 50% of maximal surface coverage) through a direct synthesis, co-condensation approach. These materials are functionalized selectively with ethynylated organic moieties through the copper-catalyzed azide alkyne cycloaddition (CuAAC) or "click" reaction. Specific loading within a material can be regulated by either the azide loading or limiting the alkyne reagent relative to the azide loading. The immobilization of ferrocene, pyrene, tris(pyridylmethyl)amine (TPA), and iron porphyrin (FeTPP) demonstrates the robust nature and reproducibility of this two step synthetic attachment strategy. Loading-sensitive pyrene fluorescence correlates with a theoretically random. surface distribution, rather than a uniform one; full site-isolation of tethered moieties *ca*. 15 Å in length. occurs at loadings less than 0.02 mmol $g^{-1}$. The effect of surface loading on reactivity is observed in oxygenation of SBA-15-[$Cu^{I}$(TPA)]. SBA-15-[$Mn^{II}$(TPA)]-catalyzed epoxidation exhibits a systematic dependence on surface loading. A comparison of homogeneous, site-isolated and site-dense complexes provides insight into catalyst speciation and ligand activity.

## Introduction

Modification of high surface area silica materials with organosilane functional groups holds considerable potential for many applications,[1–6] particularly heterogenization of discrete small molecule catalysts.[7–19] Beyond simplifying catalyst removal and recycling, heterogenization of molecular catalysts is a promising strategy to combine the selectivity of homogeneous catalysts with the stability of heterogeneous catalysts and probe reaction mechanisms. Moreover, heterogenization allows for manipulation of surface species interaction by controlling surface loadings, from site-dense to site-isolated. Site-isolation of immobilized catalysts provides potentially enhanced activity through improved substrate accessibility to the catalytic active species that are constructed with less sterically demanding ligands as potential intermolecular deactivation pathways are attenuated by limited mobility of the catalysts with regard to each other. Comparison of the reactivity of site-isolated, site-dense, and homogeneous catalysts should provide mechanistic information about the reaction of interest. A reliable synthetic method to prepare a controllable range of surface loadings would advance the rationalized screening of heterogenized, discrete catalysts.

*To whom correspondence should be addressed. stack@stanford.edu. Tel: (650) 725-8736. Fax: (650) 725-0259.

**Supporting Information Available**: Experimental section, Figures S1 and S2. This material is available free of charge via the Internet at http://pubs.acs.org.

Mesoporous silica SBA-15 are attractive candidates for catalyst supports with high surface areas (700–900 $m^2$ $g^{-1}$), large pores sizes (6–9 nm) and robust silica walls (3–6 nm).[20,21] Traditional functionalization involves hydrolytic grafting of organosilanes onto a pre-condensed silica surface, however this synthetic strategy often results in clustering of the immobilized species,[22,23] and the final coverage is highly dependent on the hydration of the surface. A more patterned distribution, which assures a minimum separation between immobilized sites, can be achieved by grafting primary amines with large protecting groups that are subsequently removed.[24,25] With this approach, the percentage of amine sites that are subsequently functionalized is sensitive to both the protecting group size and the species immobilized; varying the surface loading requires various protecting groups of different sizes.

Co-condensation of functionalized monomers during silica preparation is an alternative technique that avoids clustering found with post-synthetic grafting.[22,23] In this direct synthesis, a functionalized organosilane $(RO)_3SiR'$ is co-condensed with $(RO)_4Si$ around a templating organic polymer. The maximum concentration of functionalized organosilane that does not disrupt long-term order of the silica is dependent on the nature of the monomer.[26] By systemically controlling the mole fraction of organosilane, the surface loading can be varied from site-dense to site-isolated, and the impact of density on speciation and catalysis can be investigated.

In 2008 we reported the preparation of mesoporous silica co-condensed with organoazide functional groups.[27] The organic azide functionality attached to the mesoporous silica allows for immobilizing complexes to the surface via the high yielding and highly efficient copper-catalyzed azide alkyne cycloaddition reaction (CuAAC).[28] Azides have also been introduced into SBA materials via post-synthetic grafting.[29] CuAAC on materials prepared by both grafted and co-condensed azide-silica has been used for the immobilization of numerous biomolecules[30,31] and catalysts.[32–37]

Here we report here a more detailed examination of variably loaded azide materials prepared by a direct synthesis procedure and characterization of mesoporous SBA-15-type materials with variable and well-controlled organoazide loadings (0.2 – 8 mol% organoazide; 2 – 50% surface coverage). Attachment of four different ethynylated species to the azides probe various aspects of tether distribution.

## Results

### 1. Synthesis

**1.1 Organic Precursors—**The monomer Si-$N_3$, prepared from commercially available 3-chloropropyltriethoxysilane and $NaN_3$ (equation 2),[6,38,39] was stored in a glove box to prevent poly-siloxane formation, which could lead to a non-random distribution on the SBA-15 surface. EthynylTPA was synthesized by reductive amination of 2-formyl-5-(trimethylsilylethynyl)pyridine with dipicolylamine, followed by trimethylsilyl (TMS) deprotection of the ethynyl moiety by $K_2CO_3$/MeOH (equation 3).[40–42] Fe-ethynylTPPCl was prepared in a three-step synthesis (Scheme 1), in which the porphyrin ligand ethynyl$H_2$TPP was synthesized from 4-(3-hydroxy-3-methyl-1-butynyl)-benzaldehyde (1 equiv), benzaldehyde (3 equiv), and pyrrole (4 equiv) in refluxing propionic acid.[43] The isopropanol alkyne-protecting group dramatically changes the ligand polarity, aiding in separation via column chromatography. Deprotection occurs under a under refluxing KOH/toluene suspension.

Pyrene-Tz-*t*Bu (equation 4) and TPA-Tz-*t*Bu (equation 5) were prepared via CuAAC of the ethynylated precursors with *t*-butyl azide as homogeneous analogues to their surface immobilized species for UV-vis spectrometry and reactivity.

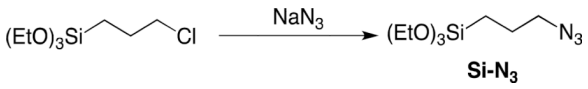


(2)

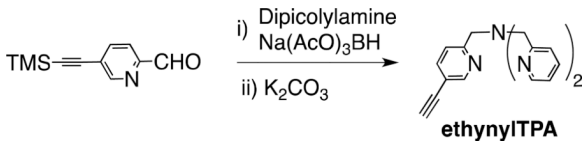


(3)

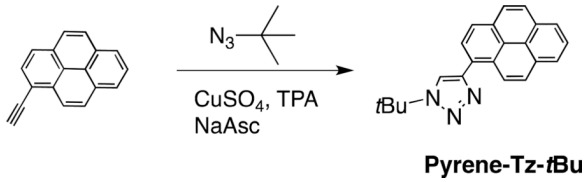


(4)

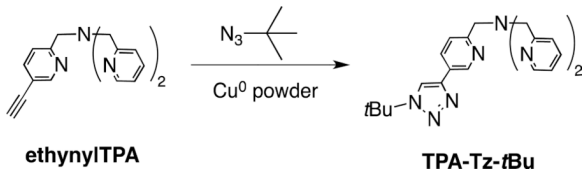


(5)

**1.2 Direct Synthesis and Characterization of SBA-15-$N_3$-*x*—**Variably loaded organoazide SBA-15 materials (SBA-15-$N_3$-*x*) were prepared by a direct synthesis procedure involving the co-condensation of defined molar ratios ($x$ = 0.2 – 8%) of Si-$N_3$ and tetraethoxyorthosilicate (TEOS) in the presence of the templating $P_{123}$ polymer in aqueous acidic (HCl) media (Scheme 2).[5,21,44,45] The template polymer was removed by Soxhlet extraction with ethanol over 24 h,[21,45] though DCS analysis and CP-MAS $^{13}C$ solid-state NMR indicate that polymer removal is not complete under these conditions.

The ordered pore structure of the SBA-15-$N_3$-*x* materials was characterized by powder X-ray diffraction (XRD) (Figure S1). The diffraction patterns of a low Si-$N_3$ loaded material, SBA-15-$N_3$-0.5, exhibit one intense and two weak diffraction peaks at 2θ = 0.85, 1.47 and 1.70°, respectively. The observed peaks correspond to the $d_{100}$, $d_{110}$, $d_{200}$ spacing of the hexagonal structure (p6mm) of the SBA material,[20] and are similar to unmodified SBA-15 (2θ = 0.85, 1.49 and 1.71°), prepared without Si-$N_3$. This indicates little change in bulk morphology by introduction of the azidosilane. With increasing Si-$N_3$ content, the $d_{100}$ diffraction peak broadens and shifts slightly. The $d_{110}$ and $d_{200}$ diffraction peaks are absent

with the highest Si-$N_3$ loading attempted (SBA-15-$N_3$-8), indicating loss in long-term order. Similar diffraction changes are reported for other modified SBA-15 type materials prepared by the co-condensation method.[21,45] The hexagonal lattice parameter $a_0$ of each SBA-15-$N_3$-*x* sample, calculated from the $d_{100}$ diffraction peak (Table 1), show similar $a_0$ values of *ca*. 12–13 nm.

$N_2$ adsorption-desorption isotherms of the SBA-15-$N_3$-*x* materials provide pore diameter and surface area information. A type IV isotherm was observed for all SBA-15-$N_3$-*x*, characteristic of mesoporous materials with narrow pore size distributions (SBA-15-$N_3$-4, Figure S2).[21,45] The average surface area (BET), pore volume, pore diameter (BJH adsorption) and wall thickness of the SBA-15-$N_3$-*x* materials were hardly changed with varying azide loading: (areas: 730 ± 30 $m^2$ $g^{-1}$, pore volumes: 0.91 ± 0.1 $cm^3$ $g^{-1}$, pore diameters: 5.7 ± 1 nm, wall thicknesses: 6.2 ± 1 nm) (Tables 1–4).

The organic functionality in the SBA-15-$N_3$-8 material was characterized by CP-MAS $^{13}C$ solid-state NMR spectroscopy (Figure 1a).[21,45] The intense signals at 54.7, 23.0, 9.5 ppm were assigned to three carbons of the azidopropyl moiety. Also observed were small signals that correspond to residual $P_{123}$ template (71, 17 ppm) and EtO-groups (59 and 17 ppm).

The azide moiety of the SBA-15-$N_3$-*x* materials was characterized by IR spectroscopy. The IR spectra of SBA-15-$N_3$-4 in Figure 2a show an intense azide stretching signal at 2110 $cm^{-1}$, in addition to Si-O-Si $\nu_{syn}$ (800 $cm^{-1}$), Si-OH ν (960 $cm^{-1}$), Si-O-Si $\nu_{as}$ (1080 $cm^{-1}$) and surface bonded $H_2O$ δ (1640 $cm^{-1}$) modes of the SBA-15 silica matrix.[16,46,47] The absorbance of the azide normalized to surface bonded water provides a spectroscopic indication of the amount of azide present in the material, and this value scales with the Si-$N_3$ molar ratio (Figure 3).

**1.3 Synthesis and characterization of SBA-15-R-*x*—**Ethynylferrocene (R = Fc), 1-ethynylpyrene (R = pyrene), ethynylTPA (R = TPA), and Fe-ethynylTPPCl (R = FeTPP) were covalently attached to SBA-15-$N_3$-*x* materials via CuAAC to yield SBA-15-R-*x*, using an excess (2 – 30 equiv) of the ethynylated species (Scheme 2).[6,15,28,39,50,51] After the reaction, the silicas were washed with a $Et_2NCS_2Na$ solution to remove any advantageously bonded copper catalyst, then rinsed with sodium acetate solution to remove excess $Et_2NCS_2Na$.

The organic functionalities in the SBA-15-R-*x* materials were characterized spectroscopically. CP-MAS $^{13}C$ solid-state NMR was employed for SBA-15-R-8 samples (R = Fc, Pyrene and TPA) (Figure 1b–d).[21,45] The spectra of SBA-15-Fc-8 shows an intense Cp ring peak at 70.6 ppm and its spinning side band signals at 134 and 9 ppm, in addition to the propyl chain with signals at 53.6, 23.7, and 9.2 ppm. The signals at 148.8 and 123.0 ppm are associated with the triazole ring. The solid state $^{13}C$ NMR resonances of SBA-15-Pyrene-8 and SBA-15-TPA-8 samples agree well with the solution $^{13}C$ NMR spectra of the homogeneous analogues Pyrene-Tz-*t*Bu and TPA-Tz-*t*Bu, respectively. SBA-15-FeTPP-*x* formation was confirmed via UV-vis spectroscopy of fluoride-digested silica samples with a 395 nm soret (B) band matching that observed with Fe-ethynylTPPCl under acidic conditions.

Porosimetry measurements of the SBA-15-R-*x* materials were performed to determine the impact of the immobilized functionality on the morphology of the bulk silica material. A representative $N_2$ adsorption-desorption isotherm of SBA-15-Pyrene-4 (Figure 2b) shows lower gas adsorption in comparison to the SBA-15-$N_3$-4 precursor, but maintains the same type IV profile. The BET surface areas, pore volumes, and pore diameters of each modified

SBA-15-R-*x* (Tables 2–4) systematically decrease with increased loading, consistent with the pores being occupied by the immobilized moieties.

Ratiometric assessment of the azide IR feature of SBA-15-R-*x* samples decreased to *ca*. 20% of its original intensity after immobilization (Figures 4 and 5). An exception is SBA-15-FeTPP-3, in which the IR feature remains *ca*. 40% of its original intensity. By comparison, only minor residual azide (less than 5%) was detected by IR following CuAAC immobilization of 1-ethynylpyrene onto an SBA-15 material that was post-synthetically grafted with azide (0.1 mmol $g^{-1}$).

The quantification of immobilized functional groups on SBA-15 materials is summarized in Table 5 and Figure 4. ICP analysis was performed on SBA-15-Fc-*x* and SBA-15-FeTPP-*x* materials,[10,52] while UV-vis spectroscopy was used for digested samples of SBA-15-pyrene-*x* and SBA-15-TPA-*x*, referenced to the homogeneous analogues Pyrene-Tz-*t*Bu and TPA-Tz-*t*Bu. For both detection methods, silica materials were digested by strongly basic conditions or *in situ* HF formation.[53] The amount of residual copper contamination from the CuAAC was also determined by ICP and was < 0.005 mmol $g^{-1}$ in all samples. For all methods of detection, the loading of organic species increased with higher Si-$N_3$ percentage. With the exception of SBA-15-FeTPP-3, materials from the same SBA-15-$N_3$-*x* gave similar loadings of organic species.

## 2. Intermolecular interaction as a function of loading

**2.1 SBA-15-Pyrene-*x*: Monomer/Eximer Fluorescence—**The fluorescence of SBA-15-Pyrene-*x* materials provides information related to the distribution and density of the pyrene groups.[24,54–57] Pyrene is an ideal probe for intermolecular interactions due to the difference in fluorescence observed for the monomeric and excimer species. At a low loading (*x* = 0.2), fluorescence is observed primarily due to the monomeric pyrene species (400 nm, Figure 5a). Higher pyrene surface loading yields increased excimer fluorescence (480 nm) relative to the monomer fluorescence, illustrating an increase in the number of intermolecular pyrene interactions. A direct correlation of loading and excimer fluorescence is observed.

Pyrene surface loading was also controlled by CuAAC onto a high azide loading SBA with the alkyne species as the limiting reagent. SBA-15-$N_3$-4 was treated with different amounts of 1-ethynylpyrene to target three different loadings: high, medium, and low (0.32, 0.12 and 0.03 mmol $g^{-1}$ SBA, respectively, Figure 5b); in all three target loadings, greater than 90% of the added pyrene is attached covalently to the surface. The high, medium, and low samples gave similar fluorescence profiles to fully treated SBA-15-pyrene-*x* of comparable loading.

A plot of the $I_{monomer}/I_{eximer}$ ratio versus surface loading for samples prepared by either method show the same trend (Figure 6). From control experiments with unfunctionalized SBA-15, simple surface physisorption can be excluded from significant contribution to the fluorescence signal with even the lowest loading samples. A low quantity of surface adsorbed pyrene (≤ 0.005 mmol $g^{-1}$) was observed after copious washing.

**2.2 Theoretical pyrene distribution—**The maximum loading of fully site-isolated pyrene can be calculated assuming an idealized hexagonal packing of circles.

$$\text{Maximum isolated loading} = \frac{S_{BET}}{2\sqrt{3}l^2 \times N_A} \quad (6)$$

where $l$ is the length of the tethered pyrene (15 Å), $S_{BET}$ is the total surface area (700 $m^2 g^{-1}$), and $N_A$ is Avogadro constant. A random distribution can be estimated by the nearest neighbor method.[58,59] The probability of nearest neighbor distances of randomly located objects within a certain area is given by following Poisson distribution function.

$$\text{Probability density function: } f(r)=2\pi\delta r\exp(-\delta\pi r^2) \tag{7}$$

$$\text{Cumulative distribution function: } F(r)=1-\exp(-\delta\pi r^2) \tag{8}$$

$$\text{Mean distance: } \bar{r}=\frac{1}{2\sqrt{\delta}} \tag{9}$$

where $r$ is the distance between the centroids of two objects (30 Å) and δ is the average surface loading (object/$Å^2$). Percent site-isolated is then calculated from equation 10.

$$\text{Site-isolated } (\%)=\exp(-\delta\pi r^2)\times 100 \tag{10}$$

### 2.2 SBA-15-TPA-*x*: Dioxygen Adduct Monomer/Dimer of CuTPA Complexes—

To probe the impact of site distribution on metal reactivity, $Cu^I$ complexes of SBA-15-TPA-*x* were treated with dioxygen (Figure 7). In homogeneous solutions, oxygenation of $[Cu^I(TPA)]^+$ generates distinctly colored species depending on the dioxygen adduct formed: a superoxo (monomeric) or peroxo (dimeric) species.[60–62] In propionitrile (EtCN), the yellow-colored solutions of $[Cu^I(TPA)]^+$ oxygenates rapidly at −90 °C to form a purple, dicopper(II), *trans*-μ-1,2-peroxo species $[(TPA)Cu^{II}\text{-}O\text{-}O\text{-}Cu^{II}(TPA)]^{2+}$.[60] At such temperatures, the monomeric superoxo species $[(TPA)Cu^{II}\text{-}O\text{-}O\bullet]^+$ is detected only transiently as a green intermediate by stopped flow methods or isolated by slow $CO/O_2$ exchange.[61,62]

The heterogenized TPA species shows similar behavior to the observed homogeneous solutions at specified loadings. Complexation of the SBA-15-TPA-*x* materials in EtCN solutions of $[Cu^I(MeCN)_4](SbF_6)$ (0.9 equiv per TPA) resulted in a color change in the materials from colorless to yellow. Oxygenation of the SBA-15-$[Cu^I(TPA)]^{+1}$-*x* materials at low temperatures afforded different observations depending on surface loading. For high loadings ($x$ = 4, 0.33 mmol $g^{-1}$), the material turned from yellow to purple, indicating the formation of a *trans*-peroxo, presumably due to the densely packed complexes. At low loadings ($x$ = 0.5, 0.06 mmol $g^{-1}$), a green color is observed, suggesting that the copper superoxide is formed and stabilized by site-isolation.

## 3. Effect of surface loading on catalysis

### 3.1 SBA-15-TPA-*x*: Epoxidation of 1-octene—

To characterize the catalytic epoxidation of terminal olefins with the immobilized SBA-15-TPA-*x* manganese complex and low acidity peracetic acid,[63] SBA-15-TPA-0.5 was first compared with the homogeneous analogue TPA-Tz-*t*Bu. In both cases, at 1:1 metal:ligand ratio and 0.1 mol% catalyst loading, epoxide yields < 20% were obtained. Most product formation is observed in the first 2 min, and the reaction is effectively complete in 5 min. The manganese concentration was then kept constant (0.1 mol%) and the amount of excess ligand was systematically increased (Figure 8). Efficient epoxidation occurs in 5 min using 1.0 mol% TPA-Tz-*t*Bu (10:1 ligand:metal, ~90 ligand TON).[64] The immobilized SBA-15-TPA-0.5

gives reactivity nearly identical to the homogeneous electronic analogue: 93% epoxide formation in 5 min with 1 mol% ligand and 0.1 mol% metal. The improved activity found with higher ratios of ligand to metal is not due to the presence of additional basic pyridine groups, as 0.1 mol% manganese, 0.1 mol% TPA and 2,6-lutidine (1 – 4 mol%) did not improve the epoxide yield. No product formation is observed in the absence of manganese.

All SBA-15-TPA-*x* materials were evaluated for epoxidation catalysis at 0.1 mol% $Mn^{II}$ salt and 1 mol% ligand to determine the effect of surface loading on the catalytic activity per ligand (Figure 9). SBA-15-TPA-0.5 gave the best results with *ca*. 85% conversion to epoxide within 2 min. Epoxide yield decreases with increasing surface loading, with SBA-15-TPA-8 yielding *ca*. 35% epoxide in the same time period. Ten min are required for SBA-15-TPA-8 to catalyze epoxide yields similar to that obtained within one min using SBA-15-TPA-0.5. A plot of epoxide yield at 2 min versus surface loading reveals a near-linear dependence on surface loading (Figure 9b).

**3.2 SBA-15-FeTPP-*x*: Carbene insertion—**Iron porphyrin catalyzed carbene insertion into a N-H bond was surveyed using piperidine and ethyl diazoacetate (EDA) (Figure 10).[65] The reaction was carried out with EDA (1.0 mmol) and a slight excess of piperidine (1.2 mmol) in $CH_2Cl_2$ with homogeneous FeTPPCl or SBA-15-FeTPP-*x* as catalysts (0.2 μmol, 0.02 mol%). In homogeneous solution, FeTPPCl catalyzed full EDA consumption over 1 h and afforded ethyl 1-piperidineacetate quantitatively (greater than 95%). Heterogeneous SBA-15-FeTPP systems also provided high yield and selectivity of the product, although longer reaction times were necessary (2 h). All catalyst loadings of SBA-15-FeTPP-*x* gave similar reaction yields; no significant relation between surface loading and reactivity was observed.

## Discussion

Controlled loading of mesoporous silica materials via CuAAC was achieved with 3-azidopropyltriethoxysilane (Si-$N_3$) as a surface tether. The propyl azide tether was chosen to allow immobilized ligands flexibility but still attenuate intermolecular interactions with neighboring ligands at high loadings. The pore size and surface area of each material, as assessed by powder X-ray diffraction and porosimetry measurements, are fully consistent with the ordered hexagonal structure of the original SBA-15 material at azide loadings less than 8%. The loss of some long-term order in SBA-15-$N_3$-8 indicates a maximum amount of Si-$N_3$ that can be co-condensed into the material. The presence of Si-$N_3$ is evident from both the CP-MAS $^{13}C$ solid-state NMR spectra[21,45] and the IR spectra. The ratio of the azide IR feature (2110 $cm^{-1}$) to surface bonded $H_2O$ bending mode (1640 $cm^{-1}$) provides a simple and rapid ratiometric assessment of the azide content.[16,46,47] These results indicate the direct synthesis of SBA-15-$N_3$-*x* provides a predictable and predefined loading of the anchor for “click” attachment onto SBA-15.

Ethynylferrocene (R = Fc), 1-ethynylpyrene (R = pyrene), ethynylTPA (R = TPA) and Fe-ethynylTPPCl (R = FeTPP) were immobilized to the surface via a CuAAC reaction with SBA-15-$N_3$-*x* to yield functionalized SBA-15-R-*x*. The porosimetry of SBA-15-R-*x* samples indicate that the mesoporous structure is retained with pore size reduction due to pore occupancy by the immobilized species. ICP evidence of only trace residual Cu (< 0.005 mmol $g^{-1}$) indicates that the copper catalysts are readily removed by $Et_2NCS_2Na$ washing.

The loading of immobilized species is controlled by the amount of azide within SBA-15-$N_3$-*x* materials, and is fairly independent of the nature of the species being attached. Although the Fc, pyrene, TPA and FeTPP materials were independently prepared under different CuAAC conditions and their surface loadings were determined by different analytical

techniques, the observed loadings all correlated closely to the Si-$N_3$ mixing ratio. Ratiometric assessment of the azide IR feature of clicked SBA-15-R-*x* samples showed *ca*. 80% decrease in azide signal, suggesting that not all alkyl azides are accessible for the CuAAC reaction when integrated into materials by co-condensation (Figures 4 and 5), possibly due to azide incorporation within inaccessible mesopores and micropores. This is consistent with the control experiment of post-synthetic Si-$N_3$ grafting, which shows > 95% azide conversion by IR. The residual 20% azide content under co-condensation preparation, however, is consistent across the materials prepared, and can be accounted for when a given loading is targeted. Only with high loadings of a bulky porphyrin species, SBA-15-FeTTP-3, do the ligand steric demands appear to have a significant impact.

Loadings can also be controlled on a dense azide SBA-15-$N_3$ surface by limiting the alkyne reagent, an attractive method if the availability of the alkyne is limited. The alkyne loadings of limited SBA-15-pyrene-4 illustrate the near quantitative nature of the CuAAC reaction on the surface, relative to alkyne substrate (Figure 5b inset). The combination of direct synthesis of SBA-15-$N_3$-*x* material followed by CuAAC attachment allows for efficient synthesis of controlled loadings of ethynlated molecules.

The distribution of immobilized species can be characterized spectroscopically. The fluorescence of pyrene is a sensitive probe into the degree of site-isolation.[24,54–57] From the experimental fluorescence observed for the SBA-15-Pyrene-*x* materials, the $I_{monomer}/I_{eximer}$ ratio dramatically changes in the 0.02–0.1 mmol $g^{-1}$ SBA range from site-isolated to site-dense. Surface distribution can be classified following three idealized arrangements: (A) clustered, (B) uniform, (C) random (Figure 11).

(A) A clustered distribution is a dense condensation of functionalized monomer during mesoporous silica formation. Clustering of the sites during direct synthesis would result in strong excimer fluorescence even at low loadings, but that behavior that is not observed.

(B) A uniform distribution maximizes the inter-species distance of the repeating object (i.e. pyrene); this distribution minimizes object overlap. Excimer fluorescence would be expected only in loadings above an overlapping limit, calculated *ca*. 0.2 mmol $g^{-1}$, assuming a 15 Å length of each surface immobilized pyrene entity and a 700 $m^2$ $g^{-1}$ surface area (equation 6). SBA-15-Pyrene-1 (0.10 mmol $g^{-1}$) and SBA-15-Pyrene-2 (0.19 mmol $g^{-1}$) both show significant excimer fluorescence, indicating that a uniform distribution is unlikely.

(C) A theoretical random distribution can be estimated by the nearest neighbor method[58,59] as a function of surface loading, using a Poisson distribution function (Figure 6). The model predicts a significant increase in monomeric species as the surface loading drops from 0.1 to 0.01 mmol $g^{-1}$. The $I_{monomer}/I_{eximer}$ ratio of SBA-15-Pyrene-0.2 (0.03 mmol $g^{-1}$), the lowest loading sample prepared, shows predominantly monomer fluorescence, suggesting a loading with site-isolation for a majority of the pyrene moieties. The correlation of a decreasing $I_{monomer}/I_{eximer}$ ratio with increasing surface loading is also consistent with the theoretical trend of randomly distributed objects. Assuming an experimental detection limit of 10% of interacting species within a material, a loading of ~ 0.02 mmol $g^{-1}$ (*ca*. 10 × the area swept by a single tethered pyrene) is needed to observe only monomer fluorescence (*c.f. ca*. 0.2 mmol $g^{-1}$ for a patterned surface). It is important to note that these estimates ignore the overestimation of BET surface area obtained from $N_2$ isotherms and that silica surfaces are irregular not flat.[66] From the above distribution study we conclude that pyrene, and therefore the original organoazide, is distributed randomly, and that spectroscopically measurable site-isolation of all attached moieties (length *ca*. 15 Å) will be achieved at loadings < *ca*. 0.02 mmol $g^{-1}$.

Limited alkyne conditions probe the selection of azide sites during the CuAAC reaction. The $I_{monomer}/I_{eximer}$ ratio tracts identically with that of excess alkyne prepared materials; the lowest limited alkyne loading (0.03 mmol $g^{-1}$) displays predominantly monomer fluorescence. Therefore, we can conclude that the CuAAC reaction randomly distributes species across the azide-decorated SBA-15 surface. This allows for a range of accessible surface densities with a singly prepared high azide loading material.

The impact of surface loading on reactivity was demonstrated through the exposure of SBA-15-[$Cu^{I}$TPA]-*x* to dioxygen. The color change of the site-dense SBA-15-[$Cu^{I}$TPA]-4 suspension (yellow to purple to pale blue) corresponds to the homogeneous $[Cu^{I}(TPA)]^{+}$ system. The localization of the color change on the silica material and a colorless solution indicates that color originates from the surface bonded [$Cu^{I}$ (TPA)] species and not leaching into solution. From the homogenous oxygenation studies of various $Cu^{I}$ complexes, thus far only two *trans*-μ-1,2- and μ-$\eta^2$:$\eta^2$- style peroxo copper(II) dimers have shown a distinct purple color.[67] In [Cu(TPA)] systems, *trans*-μ-1,2-peroxo copper(II) dimer, $[(TPA)Cu^{II}\text{-}O\text{-}O\text{-}Cu^{II}(TPA)]^{2+}$ is the only known purple-colored species.[60] From this, we conclude that a dioxygen molecule can coordinate to two closely located $Cu^{I}$ ions on the site-dense SBA-15-[$Cu^{I}$(TPA)]-4 material to form *trans*-μ-1,2-peroxo species. In contrast, the transient intermediate species of the site-isolated SBA-15-[$Cu^{I}$(TPA)]-0.5 system is green in color. Due to many $Cu^{II}$ complexes with green appearance, the oxygenated SBA-15-[Cu(TPA)]-0.5 species can not definitively be assigned from the color information alone to the mononuclear end-on superoxo species $[(TPA)Cu^{II}\text{-}O\text{-}O\bullet]^{+}$, which is short-lived in homogeneous solution.[61,62] However, the thermal sensitivity does point towards a reactive $Cu\text{-}O_2$ intermediate. While more extensive spectroscopic and reactivity characterization of these intermediates species is needed, these qualitative results do indicate that sensitive metal-based homogeneous chemistry can be translated into the mesoporous silicas through CuAAC attachment and highlights a distinct advantage of heterogenization at site-isolated loadings, namely the stabilization of reactive monomeric species.

The SBA-15-TPA-*x* materials with $Mn(CF_3SO_3)_2$ were evaluated as rapid catalysts for the epoxidation of terminal alkenes.[8,68–70] In a previous catalyst screening study, homogeneous $[Mn^{II}(TPA)]^{2+}$ was found to be a good catalyst for the epoxidation of 1-octene at 1 mol% (relative to substrate) using a low acidity peracetic acid as the oxidant, yet a poor catalyst at 0.1 mol%.[63] Oxidative ligand degradation was hypothesized as limiting overall turnover. To test this hypothesis, we have examined the yield of epoxide when keeping manganese concentration constant at 0.1 mol% and varying only the amount of ligand (Figure 8). The epoxide yield scales linearly with additional TPA-Tz-tBu, achieving > 90% epoxide with 1.0 mol% TPA ligand (10-fold ligand excess to metal, 90 ligand TON, 900 Mn TON). This enhanced reactivity is not due to a simple base effect from additional pyridine moieties from TPA, as addition of 2,6-lutidine did not improve the epoxide yield. This increasing yield with excess ligand illustrates the value in separately considering metal TON versus ligand TON, and it allows for a probe into relative ligand stability.

Low surface loading SBA-15-TPA-0.5 performs nearly identical to TPA-Tz-*t*Bu, illustrating the viability of surface immobilized TPA ligands. Both pyrene fluorescence and Cu(TPA) dioxygen adduct formation suggest a significant proportion of species on SBA-15-R-0.5 are isolated from neighboring sites, precluding interaction with neighboring complexes. The similar yields obtained with SBA-15-TPA-0.5 and TPA-Tz-*t*Bu ligands under identical concentrations suggest that Mn(TPA) dimers are not a necessary species in the catalytic cycle. Moreover, since SBA-15-TPA-0.5 shows similar ligand TON to homogeneous conditions, Mn(TPA) dimerization is unlikely the major cause of ligand deactivation at this surface loading and in solution. These observations illustrate the power of this methodology

to mechanically probe a reaction mechanism. Future modification of this ligand should therefore focus on oxidative stability over dimerization inhibition.

When the range of SBA-15-TPA-*x* materials are compared at 0.1 mol% metal and 1 mol% ligand, the epoxide yield is impacted significantly by the surface loading of the immobilized species. SBA-15-TPA-0.5 provides yields and rates most similar to homogeneous conditions, and ligand TON decreases linearly with higher surface loading. Surface crowding may impede access to the catalytic sites, and the high local concentration of TPA ligand may accelerate intermolecular deactivation pathways. It is also possible that the loss of long term order in the 8% material results in poor accessibility of immobilized TPA on the time scale of the reaction. The cause for lower yields with SBA-15-TPA-0.2 is unclear. Since enhanced reactivity with excess ligand presumes significant metal lability and transfer, it is possible a minimum surface density is required for a maximum turnover frequency. Increased interaction with surface silanol groups may also be a deactivating factor. Overall, these observations illustrate the importance of a rationally targeted surface loading versus the simple goal of maximized coverage.

To contrast the loading sensitivity of epoxidation catalysis, carbene insertion catalyzed with immobilized iron porphyrins was also probed. Compared to alkene epoxidation, carbene insertion employs mild reaction conditions, occurs at a much slower rate, and uses the FeTPP catalyst, a pre-complexed species with high stability. With homogeneous and heterogeneous FeTPP catalysts, EDA was fully consumed within 2 h at all surface densities with quantitative product and high TON. Under these conditions the impact of metal lability, ligand decomposition and site accessibility are minimized; a corresponding lack of dependence on surface loading is observed.

## Conclusion

Hybrid azidopropyl mesoporous SBA-15 (SBA-15-$N_3$-*x*) have been prepared via direct synthesis with variable azide group loadings. These hybrid silica materials retain the favorable physical attributes of the parent SBA-15 materials and allow efficient covalent attachment of ethynylated organic moieties through CuAAC immobilization. The immobilization of four distinctly different species demonstrates the robust nature of this attachment strategy. Species loading can be regulated by limiting either azide impregnation during material synthesis or alkyne concentration during CuAAC immobilization. Various immobilized functional groups provided probes to study the packing of species on the surface and the variation in nearest-neighbor as a function of surface loading.

Both metal complex speciation and catalytic epoxidation yield are sensitive to the surface loading. The ability to achieve site-isolated species is advantageous under conditions in which metal lability and ligand stability are a concern. In the case of Mn(TPA) epoxidation, the similar activity of homogeneous and site-isolated species provides insight into catalytic speciation, in a way unachievable through purely homogeneous characterization. Overall, the CuAAC attachment of homogeneous catalysts to SBA-15-$N_3$-*x* is a simple, reproducible and widely applicable strategy to prepare randomly distributed, solid-supported catalysts.

## Supplementary Material

Refer to Web version on PubMed Central for supplementary material.

## Acknowledgments

This work was financially supported in part by NIH (Grant GM70050730) and the Stanford Global. Climate and Energy Project (GCEP). J.N. acknowledges a JSPS Research Fellowship. We thank Dr. G.. Li, Dr. A. Vailionis, Dr.

R. D. Lowe, Jr., and Dr. S. Lynch at Stanford University for the ICP, XRD,. fluorescence, and solid NMR measurements, respectively.

## REFERENCES

1. Sanchez C, Julián B, Belleville P, Popall M. J. Mater. Chem. 2005; 15:3559–3592.
2. Scott BJ, Wirnsberger G, Stucky GD. Chem. Mater. 2001; 13:3140–3150.
3. Sayari A, Hamoudi S. Chem. Mater. 2001; 13:3151–3168.
4. Fuerte A, Corma A, Iglesias M, Morales E, Sánchez F. Catal. Lett. 2005; 101:99–103.
5. Peng CY, Zhang HJ, Meng QG, Li HR, Yu JB, Guo JF, Sun LN. Inorg. Chem. Commun. 2005; 8:440–443.
6. Guo ZM, Lei AW, Liang XM, Xu Q. Chem. Commun. 2006:4512–4514.
7. Zamboulis A, Moitra N, Moreau JJE, Cattoen X, Man MWC. J. Mater. Chem. 2010; 20:9322–9338.
8. Shylesh S, Jia MJ, Thiel WR. Eur. J. Inorg. Chem. 2010:4395–4410.
9. Grigoropoulou G, Christoforidis KC, Louloudi M, Deligiannakis Y. Langmuir. 2007; 23:10407–10418. [PubMed: 17764200]
10. Terry TJ, Stack TDP. J. Am. Chem. Soc. 2008; 130:4945–4953. [PubMed: 18351763]
11. Xia QH, Ge HQ, Ye CP, Liu ZM, Su KX. Chem. Rev. 2005; 105:1603–1662. [PubMed: 15884785]
12. Brulé E, de Miguel YR. Org. Biomol. Chem. 2006; 4:599–609. [PubMed: 16467931]
13. Fraile JM, García JI, Mayoral JA. Chem. Rev. 2009; 109:360–417. [PubMed: 19090693]
14. Minakata S, Komatsu M. Chem. Rev. 2009; 109:711–724. [PubMed: 19072052]
15. Collman JP, Zeng L, Wang HJH, Lei A, Brauman JI. Eur. J. Org. Chem. 2006; 12:2707–2714.
16. Lou LL, Yu K, Ding F, Peng XJ, Dong MM, Zhang C, Liu SX. J. Catal. 2007; 249:102–110.
17. Luts T, Suprun W, Hofmann D, Klepel O, Papp H. J. Mol. Catal. A. 2007; 261:16–23.
18. Tada M, Coquet R, Yoshida J, Kinoshita M, Iwasawa Y. Angew. Chem. Int. Ed. 2007; 46:7220–7223.
19. Lunn JD, Shantz DF. Chem. Commun. 2010; 46:2926–2928.
20. Zhao DY, Feng JL, Huo QS, Melosh N, Fredrickson GH, Chmelka BF, Stucky GD. Science. 1998; 279:548–552. [PubMed: 9438845]
21. Margolese D, Melero JA, Christiansen SC, Chmelka BF, Stucky GD. Chem. Mater. 2000; 12:2448–2459.
22. Kickelbick G. Angew. Chem. Int. Ed. 2004; 43:3102–3104.
23. Hoffmann F, Cornelius M, Morell J, Fröba M. Angew. Chem. Int. Ed. 2006; 45:3216–3251.
24. Hicks JC, Dabestani R, Buchanan AC, Jones CW. Chem. Mater. 2006; 18:5022–5032.
25. Hicks JC, Dabestani R, Buchanan AC, Jones CW. Inorg. Chim. Acta. 2008; 361:3024–3032.
26. Chong ASM, Zhao XS, Kustedjo AT, Qiao SZ. Micropor. Mesopor. Mater. 2004; 72:33–42.
27. Nakazawa J, Stack TDP. J. Am. Chem. Soc. 2008; 130:14360–14361. [PubMed: 18847189]
28. Rostovtsev VV, Green LG, Fokin VV, Sharpless KB. Angew. Chem. Int. Ed. 2002; 41:2596–2599.
29. Schlossbauer A, Schaffert D, Kecht J, Wagner E, Bein T. J. Am. Chem. Soc. 2008; 130:12558–12559. [PubMed: 18759397]
30. Malvi B, Sarkar BR, Pati D, Mathew R, Ajithkumar TG, Sen Gupta S. J. Mater. Chem. 2009; 19:1409–1416.
31. Huang L, Dolai S, Raja K, Kruk M. Langmuir. 2010; 26:2688–2693. [PubMed: 20141209]
32. Rana BS, Jain SL, Singh B, Bhaumik A, Sain B, Sinha AK. Dalton Trans. 2010; 39:7760–7767. [PubMed: 20657935]
33. McDonald AR, Franssen N, van Klink GPM, van Koten G. J. Organomet. Chem. 2009; 694:2153–2162.
34. McDonald AR, Dijkstra HP, Suijkerbuijk BMJM, van Klink GPM, van Koten G. Organometallics. 2009; 28:4689–4699.

35. Shi JY, Wang CA, Li ZJ, Wang Q, Zhang Y, Wang W. Chem. Eur. J. 2011; 17:6206–6213. [PubMed: 21506185]
36. Kar M, Malvi B, Das A, Panneri S, Sen Gupta S. J. Mater. Chem. 2011; 21:6690–6697.
37. Jin Z, Zhang XB, Xie DX, Gong YJ, Zhang J, Chen X, Shen GL, Yu RQ. Anal. Chem. 2010; 82:6343–6346. [PubMed: 20590097]
38. Bianco A, Maggini M, Nogarole M, Scorrano G. Eur. J. Org. Chem. 2006:2934–2941.
39. Ortega-Muñoz M, Lopez-Jaramillo J, Hernandez-Mateo F, Santoyo-Gonzalez F. Adv. Synth. Catal. 2006; 348:2410–2420.
40. Jensen MP, Lange SJ, Mehn MP, Que EL, Que L. J. Am. Chem. Soc. 2003; 125:2113–2128. [PubMed: 12590539]
41. Song JJ, Yee NK, Tan ZL, Xu JH, Kapadia SR, Senanayake CH. Org. Lett. 2004; 6:4905–4907. [PubMed: 15606096]
42. Rajadurai C, Ivanova A, Enkelmann V, Baumgarten M. J. Org. Chem. 2003; 68:9907–9915. [PubMed: 14682682]
43. Adler AD, Longo FR, Kampas F, Kim J. J. Inorg. Nucl. Chem. 1970; 32:2443–2445.
44. Luo Y, Lin J. Micropor. Mesopor. Mater. 2005; 86:23–30.
45. Alauzun J, Mehdi A, Reyé C, Corriu R. New J. Chem. 2007; 31:911–915.
46. Morey MS, O'Brien S, Schwarz S, Stucky GD. Chem. Mater. 2000; 12:898–911.
47. Brunel D, Cauvel A, Di Renzo F, Fajula F, Fubini B, Onida B, Garrone E. New J. Chem. 2000; 24:807–813.
48. Brunauer S, Emmett PH, Teller E. J. Am. Chem. Soc. 1938; 60:309–319.
49. Barrett EP, Joyner LG, Halenda PP. J. Am. Chem. Soc. 1951; 73:373–380.
50. Collman JP, Devaraj NK, Eberspacher TPA, Chidsey CED. Langmuir. 2006; 22:2457–2464. [PubMed: 16519441]
51. Rodionov VO, Presolski SI, Díaz DD, Fokin VV, Finn MG. J. Am. Chem. Soc. 2007; 129:12705–12712. [PubMed: 17914817]
52. Terry TJ, Dubois G, Murphy A, Stack TDP. Angew. Chem. Int. Ed. 2007; 46:945–947.
53. Cheng K, Landry CC. J. Am. Chem. Soc. 2007; 129:9674–9685. [PubMed: 17636908]
54. Francis C, Lin J, Singer LA. Chem. Phys. Lett. 1983; 94:162–167.
55. Lochmüller CH, Colborn AS, Hunnicutt ML, Harris JM. J. Am. Chem. Soc. 1984; 106:4077–4082.
56. Winnik FM. Chem. Rev. 1993; 93:587–614.
57. Banet P, Marcotte N, Lemer DA, Brunel D. Langmuir. 2008; 24:9030–9037. [PubMed: 18616228]
58. Cousins MA, Durose K. Thin Solid Films. 2000; 361:253–257.
59. Simberloff D. Ecology. 1979; 60:679–685.
60. Tyeklar Z, Jacobson RR, Wei N, Murthy NN, Zubieta J, Karlin KD. J. Am. Chem. Soc. 1993; 115:2677–2689.
61. Zhang C, Kaderli S, Costas M, Kim E, Neuhold Y, Karlin K, Zuberbühler AD. Inorg. Chem. 2003; 42:1807–1824. [PubMed: 12639113]
62. Maiti D, Fry HC, Woertink JS, Vance MA, Solomon EI, Karlin KD. J. Am. Chem. Soc. 2007; 129:264–265. [PubMed: 17212392]
63. Murphy A, Stack TDP. J. Mol. Catal. A. 2006; 251:78–88.
64. Underivatized TPA performs slightly better, requiring 7:1 ligand:metal to achieve > 90% epoxide yield in 5 min
65. Baumann LK, Mbuvi HM, Du G, Woo LK. Organometallics. 2007; 26:3995–4002.
66. Avnir D. J. Am. Chem. Soc. 1987; 109:2931–2938.
67. Mirica LM, Ottenwaelder X, Stack TDP. Chem. Rev. 2004; 104:1013–1045. [PubMed: 14871148]
68. Ottenbacher RV, Bryliakov KP, Talsi EP. Adv. Synth. Catal. 2011; 353:885–889.
69. Wortmann R, Florke U, Sarkar B, Umamaheshwari V, Gescheidt G, Herres-Pawlis S, Henkel G. Eur. J. Inorg. Chem. 2011:121–130.
70. Hao ER, Wang ZY, Jiao LJ, Wang SW. Dalton Trans. 2010; 39:2660–2666. [PubMed: 20179861]

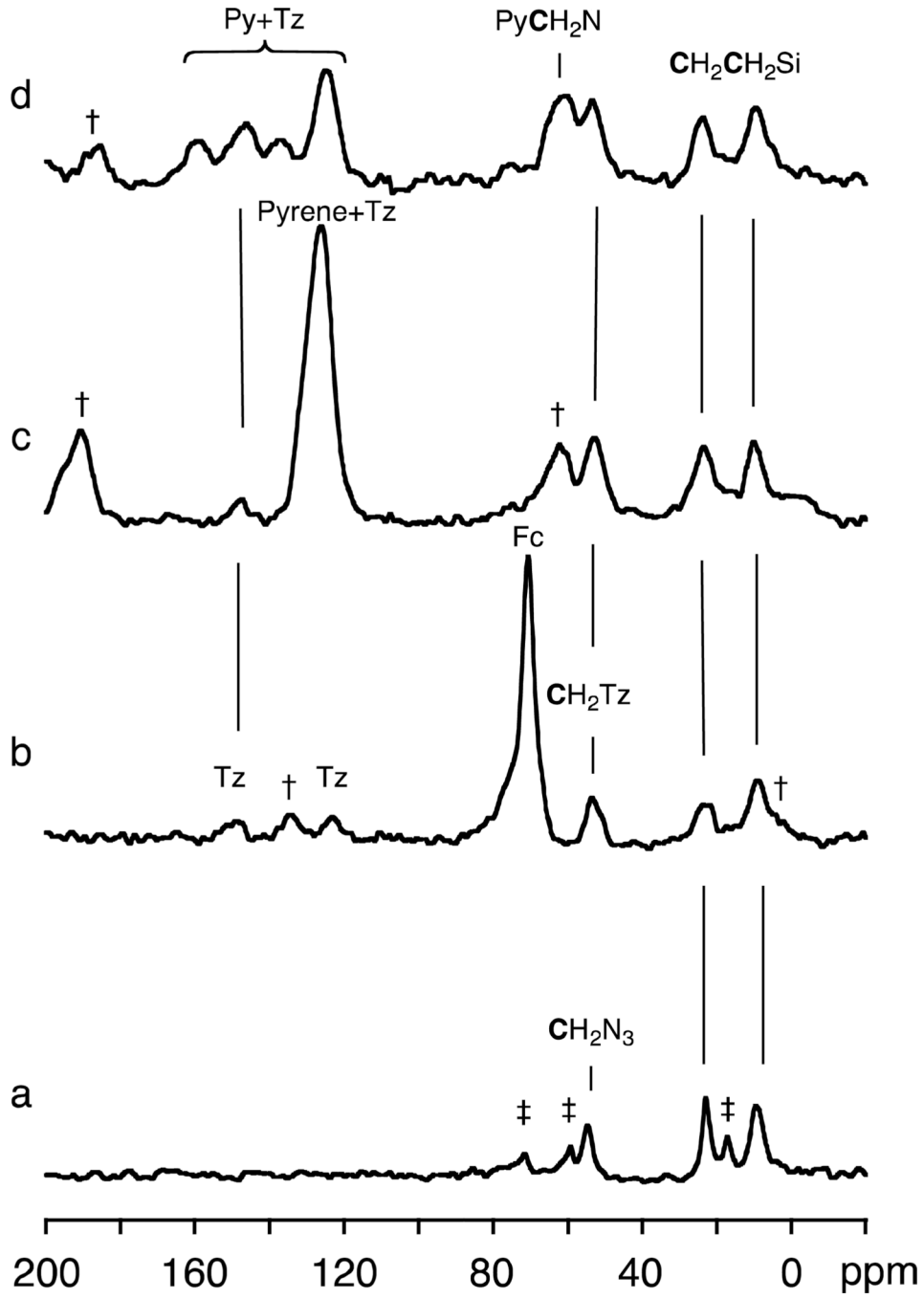


**Figure 1.**
CP-MAS $^{13}C$ solid-state NMR of (a) SBA-15-$N_3$-8, (b) SBA-15-Fc-8, (c) SBA-15-Pyrene-8, and (d) SBA-15-TPA-8. †: spinning side band signals, ‡: residual $P_{123}$ template and solvent EtOH / EtO-Si group, Fc: ferrocene ring, Py: pyridine group, Tz: triazole group.

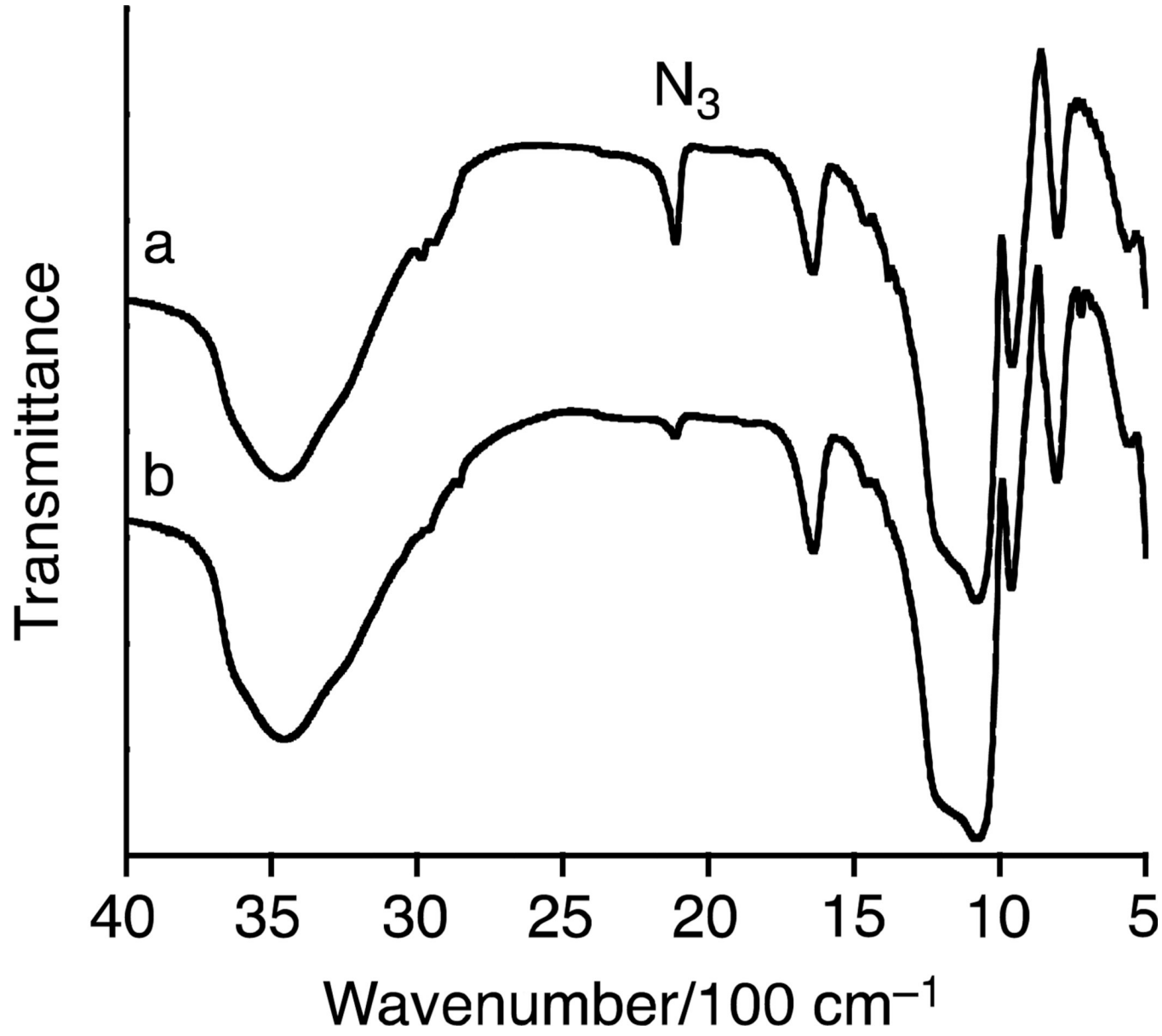


**Figure 2.**
IR spectra of (a) SBA-15-$N_3$-4, and (b) SBA-15-Pyrene-4 in a KBr pellet.

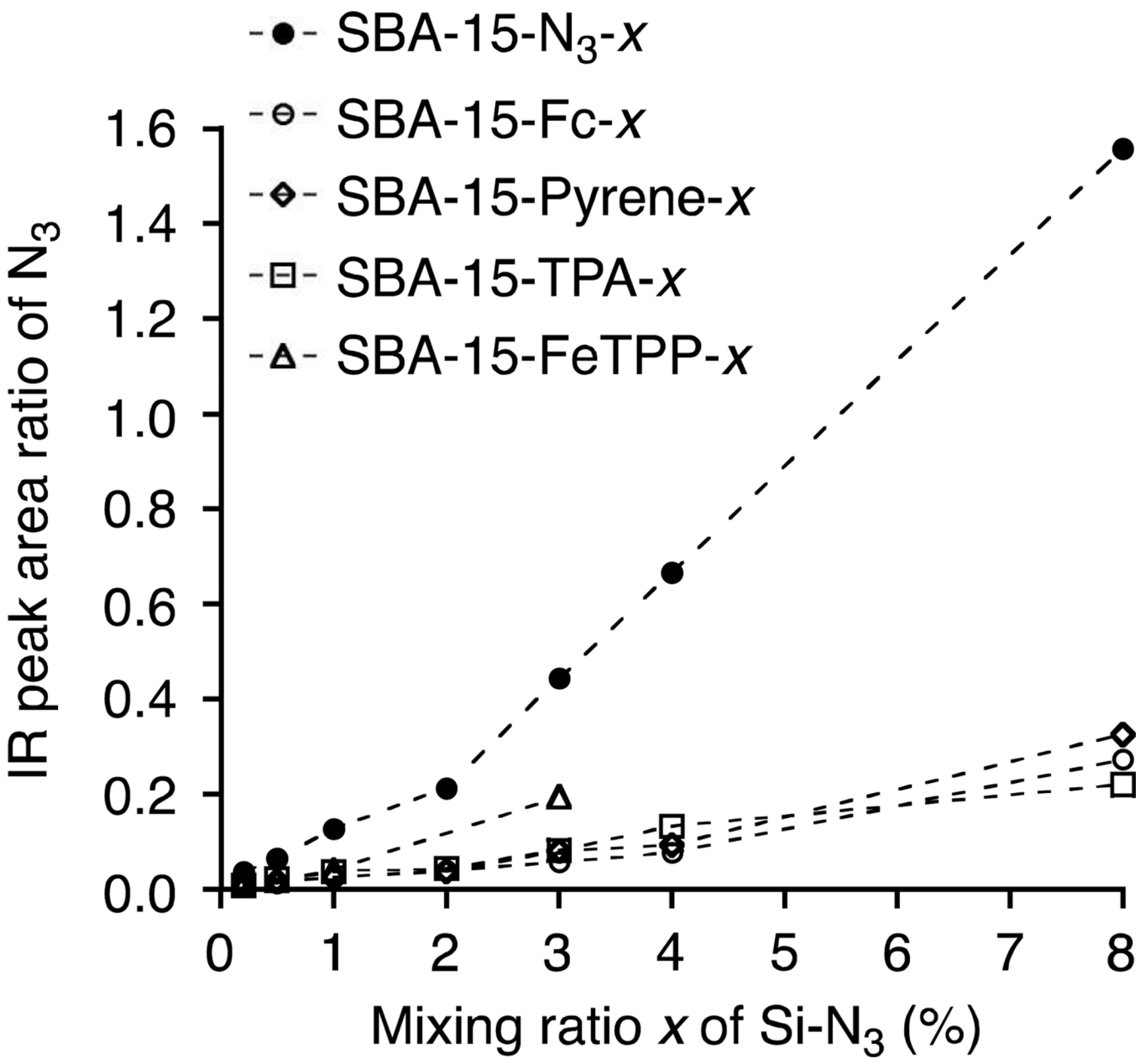


**Figure 3.**
IR peak area of azide (2110 $cm^{-1}$ normalized to the signal at 1640 $cm^{-1}$) of the SBA-15-$N_3$-*x* and SBA-15-R-*x* materials as a function of the mixing ratio *x* of Si-$N_3$.

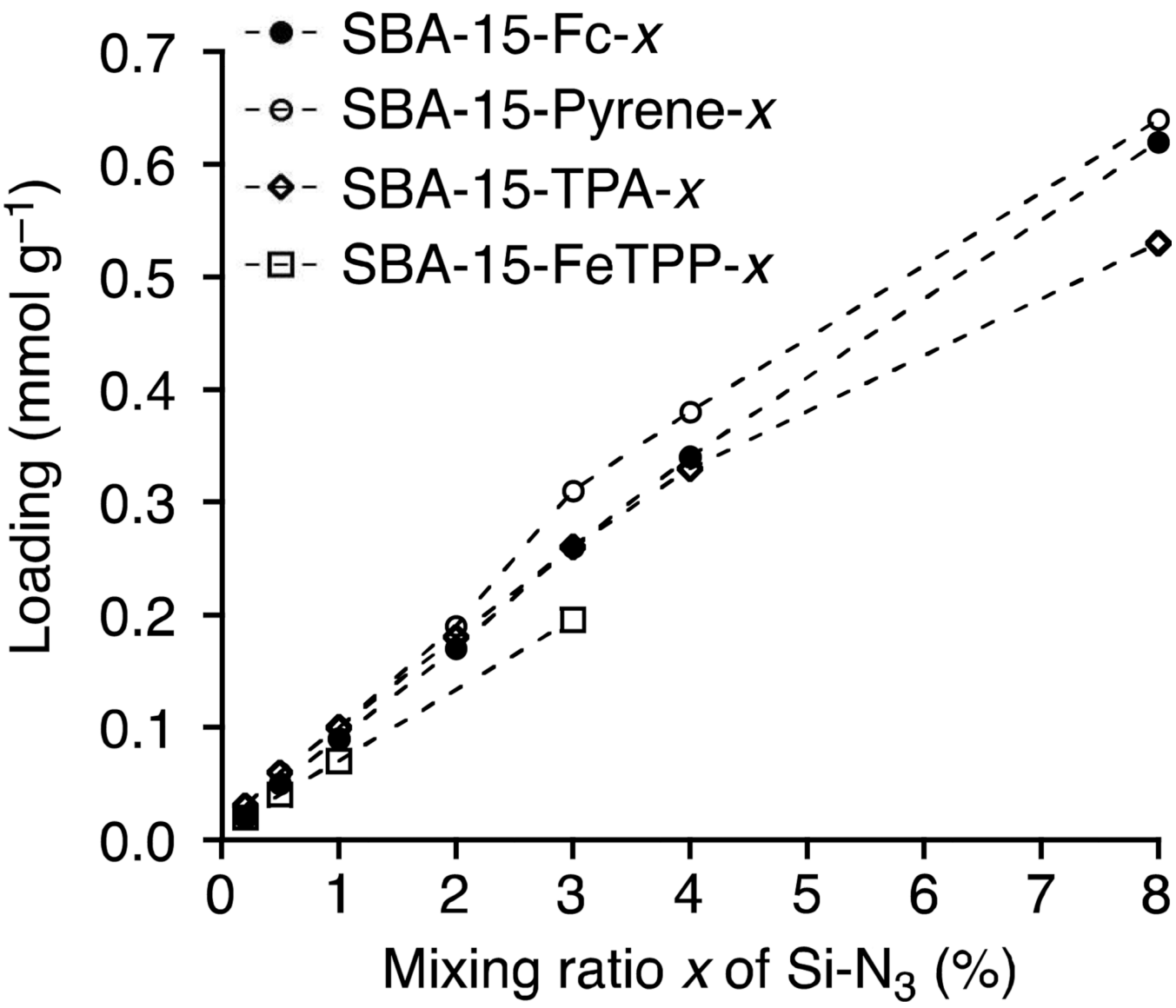


**Figure 4.**

Loadings (mmol $g^{-1}$) of SBA-15-R-*x* (R: Fc, Pyrene, TPA and FeTPP) as a function of the mixing ratio *x* of Si-$N_3$. Fc and FeTPP loadings were determined by ICP analysis of digested samples. Pyrene and TPA loadings were determined by UV-vis spectrometry of digested samples.

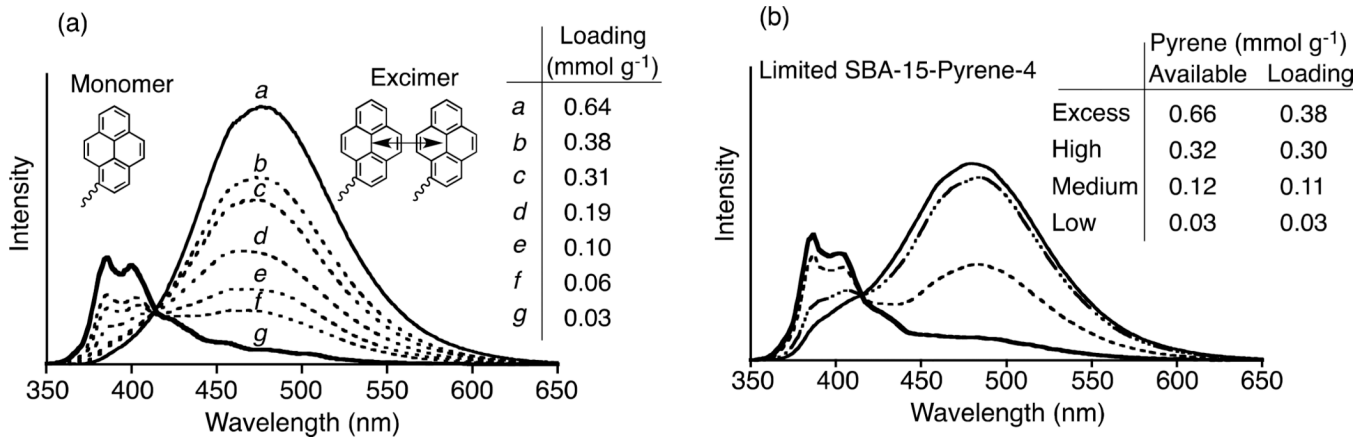


**Figure 5.**

(a) Fluorescence spectra of (a) SBA-15-Pyrene-*x* (*x* = 8, 4, 3, 2, 1, 0.5, 0.2 mol%) and (b) limited alkyne SBA-15-Pyrene-4. Inset are loadings of pyrene. SBAs were suspended in $CHCl_3$ with continuous stirring ($\lambda_{ex}$ = 330 nm). For visual comparison, the spectra were normalized at 415 nm.

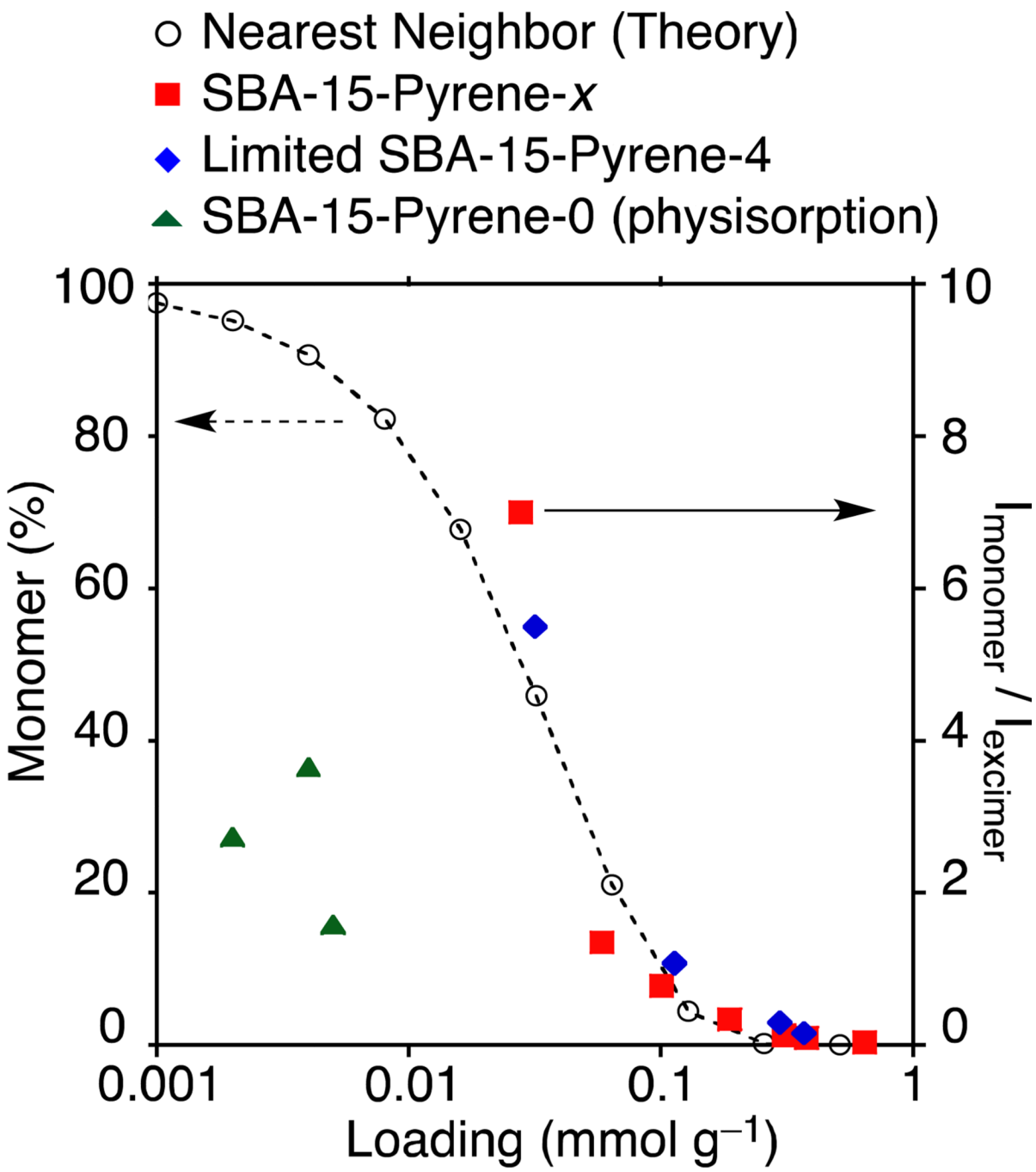


**Figure 6.**

Comparison of a theoretically random distribution and observed pyrene fluorescence ratio. Open circle values are estimates of monomer amount (%) using a nearest neighbor method ($S_{BET}$ = 700 $m^2$ $g^{-1}$ and tether length $l$ = 15 Å). Filled shape values are experimental results of the $I_{monomer}/I_{eximer}$ ratio of SBA-15-Pyrene-*x* (filled square, right), limited alkyne SBA-15-Pyrene-4 (filled diamond, right), and unfunctionalized SBA-15 exposed to 1-ethynylpyrene (filled triangle, right).

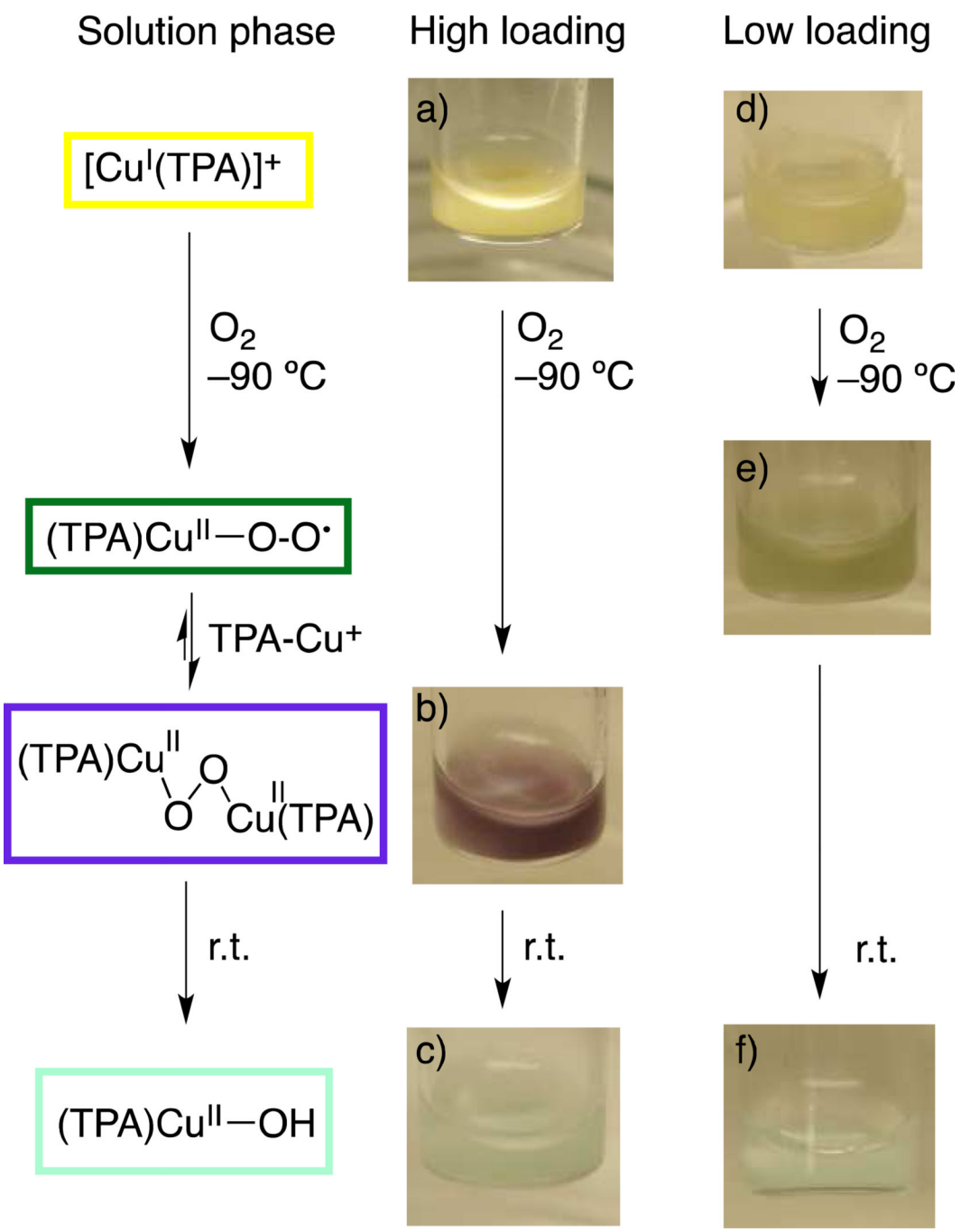


**Figure 7.**
Color changes upon oxygenation of SBA-15-TPA-4 (a–c) and SBA-15-TPA-0.5 (d–f) with 0.9 equiv of $[Cu^{I}(MeCN)](SbF_6)$ in EtCN at −90 °C. Characteristic colors of intermediates in the corresponding homogeneous solutions are displayed to the left.

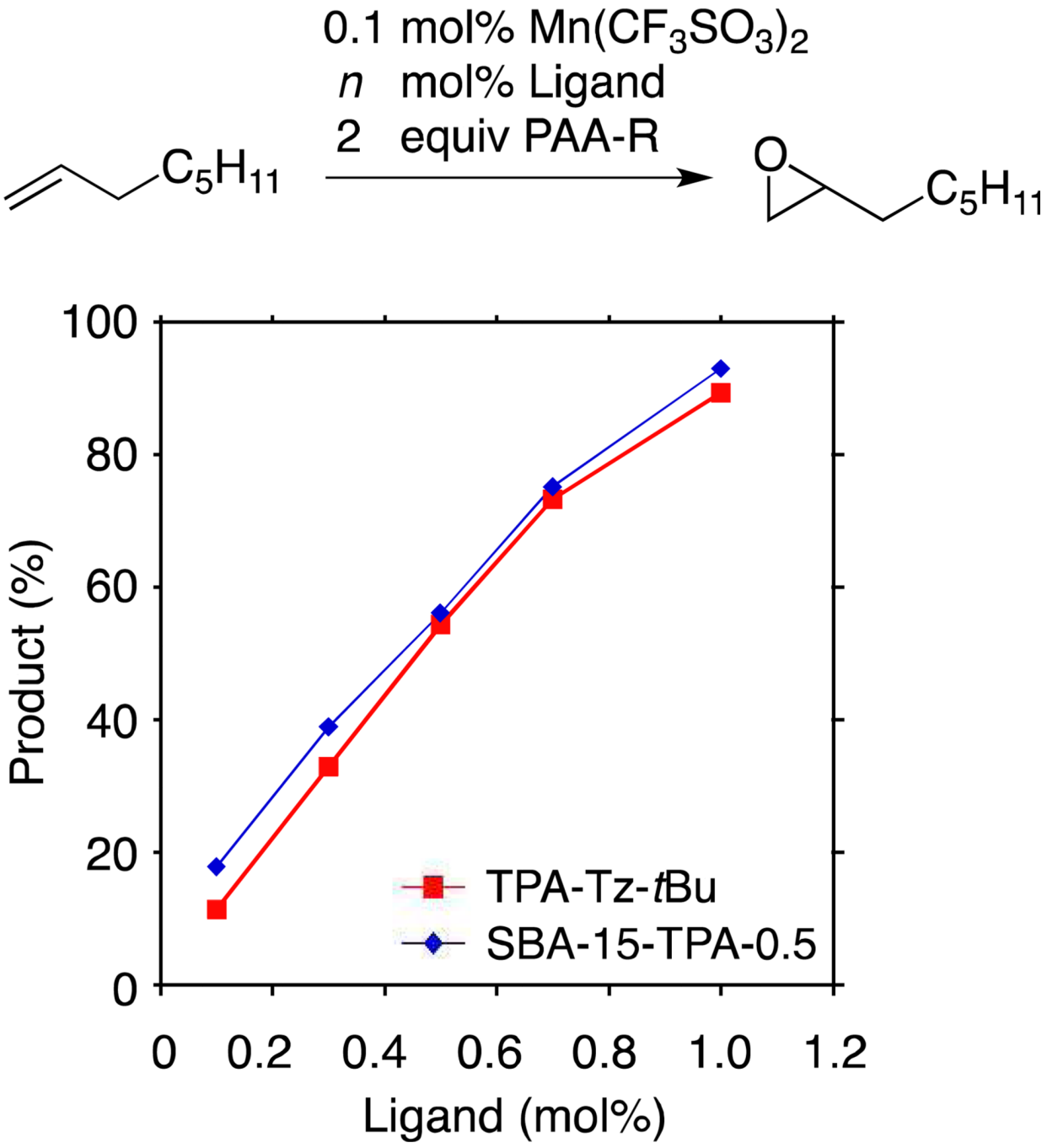


**Figure 8.**
Epoxidation of 1-octene, 0.25 M in HOAc, RT in 5 min. In all cases, manganese content is 0.1 mol% and the mol% of ligand is varied.

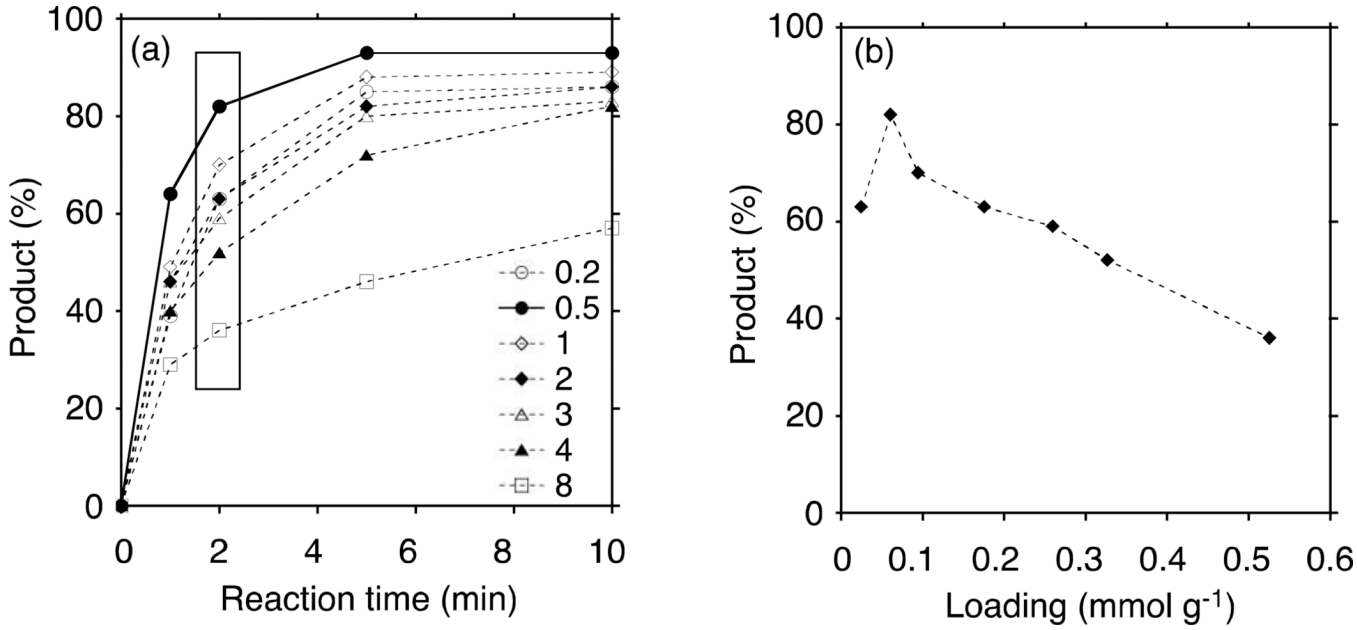


**Figure 9.**
(a) Time dependence of the epoxidation of 1-octene with $Mn(CF_3SO_3)_2$ (0.1 mol%), SBA-15-TPA-*x* (1 mol%) and PAA-R (2 equiv). (b) Epoxide yield at 2 min relative to TPA surface loading (boxed data points in a).

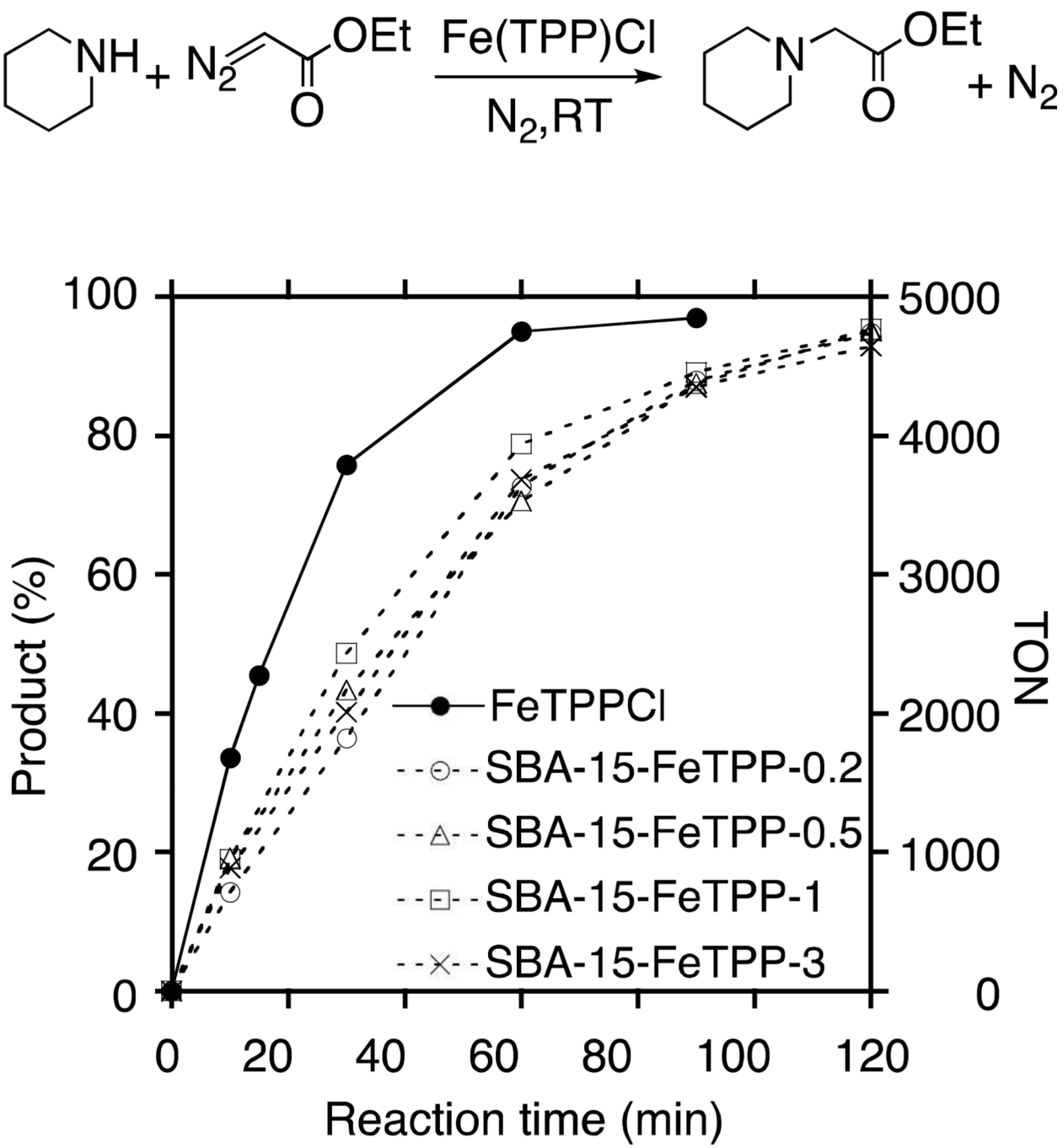


**Figure 10.**
Time dependence of the formation of ethyl 1-piperidineacetate from EDA (1.0 mmol) and piperidine (1.2 mmol) with homogeneous and heterogeneous FeTPP catalysts (0.02 mol% in all cases).

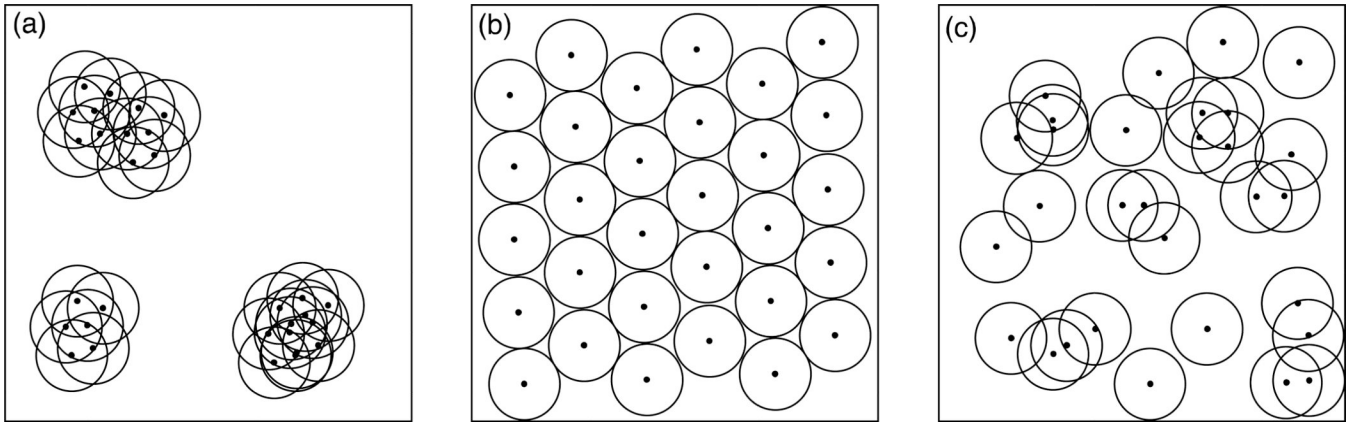


**Figure 11.**
Graphical representations of theoretical surface distributions: (a) clustered, (b) uniform, (c) random.

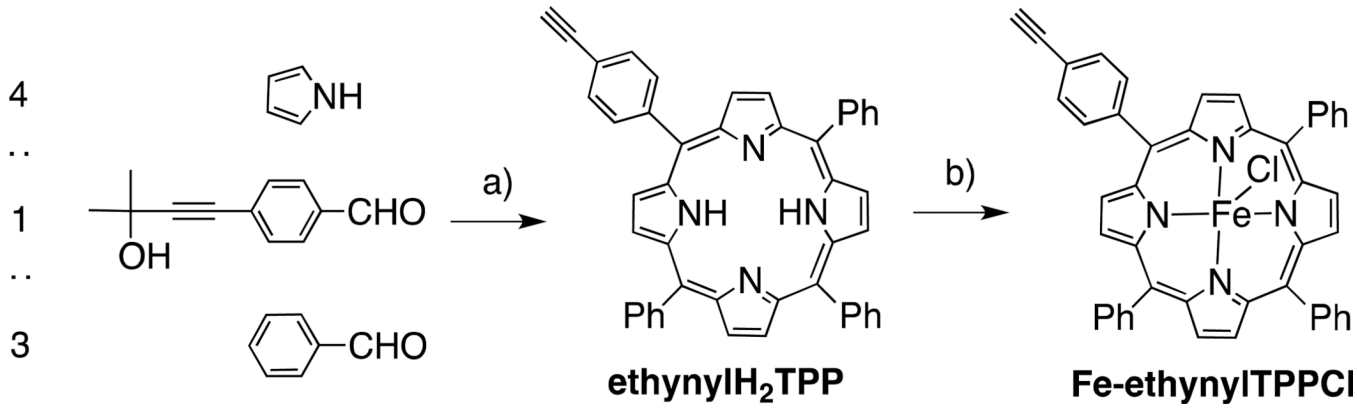


**Scheme 1.**

a) Refluxing propionic acid, 3 h, followed by KOH in refluxing toluene for 4 h. (11% overall yield) b) $FeCl_2$ in DMF, 1 h. (85% yield)

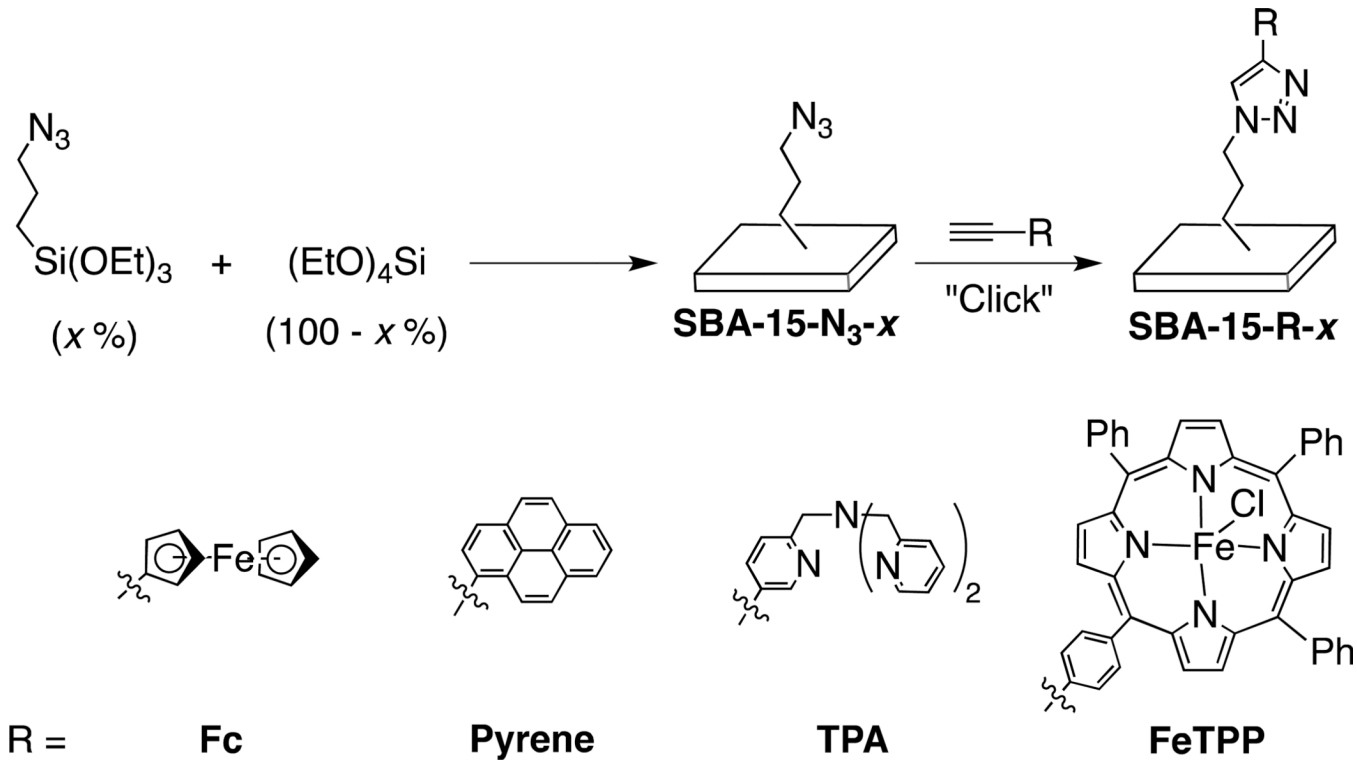


**Scheme 2.**
Preparation of surface modified mesoporous silicas, SBA-15-R-*x*.

**Table 1**

XRD diffraction peaks 2θ, lattice parameters $a_0$, and wall thickness $d_w$ of unfunctionalized SBA-15 and SBA-15-$N_3$-$x$ samples.

| | (100) (°) | (110) (°) | (200) (°) | $a_0$ (nm)[a] | $d_w$ (nm)[b] |
|---|---|---|---|---|---|
| SBA-15 | 0.851 | 1.486 | 1.711 | 12.0 | 5.4 |
| SBA-15-$N_3$-$x$ | | | | | |
| $x$ = 0.2 | 0.765 | 1.330 | 1.535 | 13.3 | 6.7 |
| 0.5 | 0.850 | 1.470 | 1.680 | 12.0 | 6.9 |
| 1.0 | 0.805 | 1.400 | 1.570 | 12.7 | 6.6 |
| 2.0 | 0.846 | 1.471 | 1.686 | 12.1 | 6.0 |
| 3.0 | 0.856 | 1.491 | 1.736 | 11.9 | 6.9 |
| 4.0 | 0.856 | 1.496 | 1.726 | 11.9 | 6.7 |
| 8.0 | 0.965 | -[c] | -[c] | 10.6 | 5.9 |

[a] $a_0 = 2d_{100} / \sqrt{3}$.

[b] $d_w = a_0 - D_p$, where $D_p$ is the mesopore average diameter.

[c] Too broad to identify.

**Table 2**

BET surface areas $S_{BET}$ ($m^2\ g^{-1}$) of functionalized SBA-15 materials.[a]

| | *x* = | | | | | | | |
|---|---|---|---|---|---|---|---|---|
| **SBA-15-R** | **0** | **0.2** | **0.5** | **1.0** | **2.0** | **3.0** | **4.0** | **8.0** |
| $N_3$-*x* | 710[b] | 740 | 742 | 704 | 750 | 759 | 734 | 731 |
| Fc-*x* | | 480 | 572 | 502 | 483 | 404 | 386 | 273 |
| Pyrene-*x* | | 523 | 598 | 450 | 507 | 404 | 269 | 198 |
| TPA-*x* | | 639 | 399 | 444 | 389 | 340 | 288 | 151 |
| FeTPP-*x* | | 670 | 676 | 436 | _[c] | 378 | _[c] | _[c] |

[a] Determined by the BET method[48] from the adsorption branch.

[b] Unfunctionalized SBA-15.

[c] The sample was not prepared.

**Table 3**

Pore volumes $V_p$ ($cm^3\ g^{-1}$) of functionalized SBA-15 materials.[a]

| | *x* = | | | | | | | |
|---|---|---|---|---|---|---|---|---|
| **SBA-15-R** | **0** | **0.2** | **0.5** | **1.0** | **2.0** | **3.0** | **4.0** | **8.0** |
| $N_3$-*x* | 0.84[b] | 1.01 | 0.98 | 0.97 | 0.96 | 0.83 | 0.84 | 0.82 |
| Fc-*x* | | 0.87 | 0.75 | 0.87 | 0.73 | 0.50 | 0.47 | 0.29 |
| Pyrene-*x* | | 1.07 | 0.73 | 0.84 | 0.72 | 0.52 | 0.38 | 0.21 |
| TPA-*x* | | 0.84 | 0.79 | 0.73 | 0.63 | 0.49 | 0.41 | 0.18 |
| FeTPP-*x* | | 0.80 | 0.81 | 0.54 | _[c] | 0.30 | _[c] | _[c] |

[a] Determined by the BJH method[49] from the adsorption branch.

[b] Unfunctionalized SBA-15.

[c] The sample was not prepared.

**Table 4**

Pore diameters $D_p$ (nm) of functionalized SBA-15 materials.[a]

| | *x* = | | | | | | | |
|---|---|---|---|---|---|---|---|---|
| **SBA-15-** | **0** | **0.2** | **0.5** | **1.0** | **2.0** | **3.0** | **4.0** | **8.0** |
| $N_3$-*x* | 6.6[b] | 6.6 | 5.1 | 6.1 | 6.1 | 5.0 | 5.2 | 4.7 |
| Fc-*x* | | 6.7 | 4.7 | 6.4 | 5.3 | 5.1 | 5.0 | 3.6 |
| Pyrene-*x* | | 7.0 | 5.0 | 6.7 | 5.2 | 5.2 | 5.1 | 3.5 |
| TPA-*x* | | 6.6 | 5.3 | 5.5 | 5.3 | 5.1 | 4.7 | 3.8 |
| FeTPP-*x* | | 6.7 | 5.8 | 6.5 | _[c] | 5.6 | _[c] | _[c] |

[a] Determined by the BJH method[49] from the adsorption branch.

[b] Unfunctionalized SBA-15.

[c] The sample was not prepared.

*J Am Chem Soc*. Author manuscript; available in PMC 2013 February 8.

**Table 5**

Loading of compounds and [residual Cu] (mmol $g^{-1}$) of functionalized SBA-15 materials.[a]

| | ***x*** **=** | | | | | | |
|---|---|---|---|---|---|---|---|
| **SBA-15-R** | **0.2** | **0.5** | **1.0** | **2.0** | **3.0** | **4.0** | **8.0** |
| Fc-*x* | 0.02 | 0.05 | 0.09 | 0.17 | 0.26 | 0.34 | 0.62 |
| | [0.003] | [0.003] | [0.003] | 0.002] | [0.002] | [0.005] | [0.003] |
| Pyrene-*x* | 0.03 | 0.06 | 0.10 | 0.19 | 0.31 | 0.38 | 0.64 |
| | [0.002] | [0.001] | [0.001] | 0.002] | [0.001] | [0.001] | [0.001] |
| TPA-*x* | 0.02 | 0.06 | 0.10 | 0.18 | 0.26 | 0.33 | 0.53 |
| | [0.001] | [0.001] | [0.001] | 0.002] | [0.001] | [0.001] | [0.003] |
| FeTPP-*x* | 0.02 | 0.04 | 0.07 | _[b] | 0.15 | _[b] | _[b] |
| | [0.002] | [0.004] | [0.006] | - | [0.004] | - | - |

[a] Fc, FeTPP and Cu loadings were determined by ICP analysis. Pyrene and TPA loadings were determined by UV-vis spectrometry.

[b] The sample was not prepared.